Overcoming the natural excitation assumption: a strategy to deal with colouration and time/space correlation in output-only modal analysis

S. De Carolis, G. De Filippis, D. Palmieri, L. Soria
Politecnico di Bari, Department of Mechanics, Mathematics and Management DMMM,
Via Edoardo Orabona 4, 70126 Bari, Italy

Abstract
The main drawback of the Operational Modal Analysis (OMA) approach consists in the natural excitation (NExT) assumption of uncorrelated white noise excitations. These hypotheses are violated in all those cases in which the exerted environmental loads exhibit colouration, harmonic content or some kind of correlation, with regards to mechanical engineering systems like vehicles during road tests or operating wind turbines. Specifically, we propose a generalized OMA framework with the aim to overcome this limitation. The generalized modal structures of the output power spectral densities (PSDs) are derived, as models showing the dependence not only by the modal parameters, but also by the input spectral characteristics, and employed in a customized identification technique. The proposed formulation is compared with the classical one, by performing modal parameter estimation of an experimental slender beam under operating loading conditions, comprising a number of NExT assumption infringements.

1 Introduction

The NExT assumption is often valid in case of civil engineering structures like buildings, bridges, and towers because they are mainly excited by seismic micro-tremors, wind or traffic, which are faithful to the statistical description of stationary Gaussian uncorrelated white noises. By dealing with mechanical engineering structures, the operational environment could offer ambient forces which infringe classical OMA hypothesis due to the presence of harmonic components (from moving/rotating parts of the machine like gears, shafts, couplings, reciprocating piston in pumps and engines, etc.), non-white excitation [1] (e.g. forces induced on vehicles by road surface roughness [2, 3, 4, 5, 6], wind speed fluctuation, i.e. turbulence, in wind turbines [7]), the existence of temporal and/or spatial correlation between loads (as the wheelbase filtering effect in vehicle dynamics [8, 9, 10]), and time periodic effects in rotating systems [11]. These aspects can give rise to OMA methods' failures: for instance, harmonic components may be identified as spurious resonance modes (also called operational modes) or they can affect the estimation of modal parameters, especially resulting in poor damping ratio estimations. Many approaches have been proposed over the years to address this lack of description in OMA [12]: (i) statistics-driven identification of harmonics where statistical measurement known as probability density function and kurtosis are used to determine whether a peak in a spectrum is an operational or natural mode [13]; (ii) removal of harmonic components from the signal in pre-processing stage [14, 15, 16]; (iii) explicit incorporation of the harmonic component in existing OMA methods for the identification of modal parameters, assuming a prior knowledge of the harmonic frequencies [17, 18]; (iv) input spectrum independent techniques, such as the transmissibility-based OMA (TOMA) and polyreference TOMA (p-TOMA) [19, 20], which handle the problem when ambient excitation is not white. In addition, a hybrid approach using elements of both EMA and OMA was proposed by [21] called OMAX (i.e. Operational Modal Analysis in presence of eXogenous inputs): it is based on a system model that takes both the measured and the ambient excitation into account directly to the measured signals [22, 23]. In the recent years, the development of methods aiming at overcoming the NExT assumption limitations has become a challenging topic [24, 25, 26]. Looking for a method suitable mechanical application such as vehicle systems

running on a straight road with a constant speed and rotating wind turbines [27], authors started to modify the classical OMA methods to achieve specialized techniques or they introduced specific transformations as a data pre-processing aimed at extending operational modal analysis to linear, periodically time-varying systems. Time periodic effects in wind turbines might arise due to interaction between the flow around the blade and tower or variation in the wind speed with altitude. Forward Coleman transformation (also called multi-blade coordinate transformation, MBC) or harmonic transfer function concept [28] is, for instance, applied to the data measured on the wind turbine blades, then combined with tower responses, in order to apply Operational Modal Analysis to the transformed data. Furthermore, an analytical expression for the output spectrum in terms of the modal parameters was developed and used to interpret the spectra [11]. Analogously, the idea to perform OMA on vehicles during road tests is prevented by some other infringements of the NExT assumption [29]. In fact, a certain correlation among the road forces acting on the wheels arises: different kinds of correlation exist which describe relation between loads on the front and the rear axle, or inputs on wheels belonging to the left and the right side [10]. This aspect, combined with typical high damped rigid body modes, make challenging the application of standard OMA algorithms. In [30], the smooth orthogonal decomposition, SOD, method is extended to the modal parameter estimation (MPE) of lightly damped systems, in which the inputs are time shifted functions (i.e. temporal correlated) of white noise signals. This approach has been proposed to identify the modal parameters of a vehicle during road testing, but, although the assumption of time correlated inputs is well addressed, relatively inaccurate results have been obtained owing to the drawbacks of time-domain techniques when treating highly damped systems. On the other hand, in [31] vertical accelerations of unsprung masses are used as inputs for subspace identification, giving comparably accurate results with the subspace identification method using tyre forces as inputs. Recently, a specialised modal model, referred to as the Track-Vehicle Interaction Modal Model (TVIMM), able to incorporate the character of road/rail inputs acting on vehicles during operation, is developed together with a method for determining the modal parameters of road and rail vehicles [32, 33]. The idea, behind the hereby called generalized OMA (G-OMA), consists in overcoming a number of NExT assumption infringements by including a priori known input correlation features in the OMA modal structures [34, 35]. In this sense, an analytical description of these effects (such as coloration, time correlation, spatial coherence, etc.) is needed and explicated in the models employed by the identification techniques. This way, it is possible to perform "ad hoc" procedures, even in case of completely violation of the classical assumption and still not measuring forces.

The rest of the paper is organized as follows. In Section 2, the theoretical background of G-OMA is presented regarding the modal model of the output PSD matrix and the two step identification strategy is supplied. In Section 3 an experimental case study is exploited evaluating the performance of the G-OMA procedure with respect to the classical OMA approach. Finally, Section 4 summarizes the main conclusions of this work.

2 No-NExT OMA

By considering a linear, time-invariant, damped, vibrating system having N degrees of freedom (dofs), the relevant system transfer function matrix is defined as the inverse of the dynamic stiffness $\mathbf{B}(s)$

$$\mathbf{H}(s) = (s^2\mathbf{M} + s\mathbf{C} + \mathbf{K})^{-1} = \mathbf{B}(s)^{-1}, \tag{1}$$

with s the Laplace variable, $\mathbf{M}$, $\mathbf{C}$, and $\mathbf{K} \in \mathbb{R}^{N\times N}$ are the mass, damping, stiffness matrices. From the modal analysis theory [36], the modal decomposition of the frequency response function matrix, FRF, is

$$\mathbf{H}(\mathrm{i}\omega) = \sum_{n=1}^{N} \frac{\boldsymbol{\psi}_n \boldsymbol{L}_n^{\mathrm{T}}}{\mathrm{i}\omega - \lambda_n} + \frac{\boldsymbol{\psi}_n^* \boldsymbol{L}_n^{\mathrm{H}}}{\mathrm{i}\omega - \lambda_n^*} = \sum_{n=1}^{2N} \frac{\boldsymbol{\psi}_n \boldsymbol{L}_n^{\mathrm{T}}}{\mathrm{i}\omega - \lambda_n}, \tag{2}$$

where a translate into the Fourier domain is done by imposing $s = \mathrm{i}\omega$, with λ_n and $\boldsymbol{\psi}_n \in \mathbb{C}^{N\times 1}$ as the system poles and mode shapes, and $\boldsymbol{L}_n = Q_n \begin{bmatrix}\psi_{1,n} & \cdots & \psi_{L,n}\end{bmatrix} \in \mathbb{C}^{L\times 1}$ indicating the modal participation vector related to the n-th pole containing the L components of the n-th mode shape where the L external forces act ($Q_n = 1/m_{an}$ is referred as scale factor).

2.1 Classical PSD modal model

The power spectral density (PSD) matrix $\mathbf{S}^q(\mathrm{i}\omega) \in \mathbb{C}^{N\times N}$ referred to the system outputs can be evaluated by using the following implicit analytical expression, the well-known input-output formula, holding in the frequency domain [37]

$$\mathbf{S}^q(\mathrm{i}\omega) = \mathbf{H}(\mathrm{i}\omega)\mathbf{S}^f(\mathrm{i}\omega)\mathbf{H}(\mathrm{i}\omega)^{\mathrm{H}}, \tag{3}$$

where $\mathbf{S}^f(\mathrm{i}\omega) \in \mathbb{C}^{L\times L}$ is the Fourier transform of the input correlation matrix. Substituting in Eq. (3) the modal decomposition of Eq. (2), one obtains

$$\mathbf{S}^q\left(\mathrm{i}\omega\right) = \left(\sum_{n=1}^{2N} \frac{\boldsymbol{\psi}_n \boldsymbol{L}_n^{\mathrm{T}}}{\mathrm{i}\omega - \lambda_n}\right) \mathbf{S}^f\left(\omega\right) \left(\sum_{m=1}^{2N} \frac{\boldsymbol{L}_m \boldsymbol{\psi}_m^{\mathrm{T}}}{-\mathrm{i}\omega - \lambda_m}\right). \tag{4}$$

So, from that perspective, the assumption of inputs as white uncorrelated noises,i.e. the NExT hypothesis, here becomes

$$\mathbf{S}^f(\mathrm{i}\omega) = \begin{bmatrix} \alpha_1 & \cdots & 0 \\ \vdots & \ddots & \vdots \\ 0 & \cdots & \alpha_L \end{bmatrix}, \tag{5}$$

with α_i a real-valued constant, implying the following partial fraction decomposition the matrix in Eq. (4)

$$\mathbf{S}^q\left(\mathrm{i}\omega\right) = \sum_{n=1}^{2N} \frac{\mathbf{R}_n^+}{\mathrm{i}\omega - \lambda_n} + \frac{\mathbf{R}_n^-}{-\mathrm{i}\omega - \lambda_n}, \tag{6}$$

where the resulting residue matrix is

$$\mathbf{R}_n^+(\mathrm{i}\omega) = \boldsymbol{\psi}_n \boldsymbol{\rho}_n^{\mathrm{T}}, \tag{7}$$

and the definition of operational reference vector coming up again as

$$\boldsymbol{\rho}_n(\mathrm{i}\omega)^{\mathrm{T}} = \boldsymbol{L}_n^{\mathrm{T}} \mathbf{S}^f\left(\mathrm{i}\omega\right) \left(\sum_{m=1}^{2N} \frac{\boldsymbol{L}_m \boldsymbol{\psi}_m^{\mathrm{T}}}{-\lambda_n - \lambda_m}\right) = \sum_{g=1}^{L} \alpha_g \boldsymbol{g}_n^{gg\mathrm{T}}, \tag{8}$$

with

$$\boldsymbol{g}_n^{gg} = \frac{\psi_{gn}}{m_{an}} \sum_{m=1}^{2N} \frac{\psi_{gm}}{m_{am}\left(-\lambda_n - \lambda_m\right)} \boldsymbol{\psi}_m, \tag{9}$$

Therefore, by assuming the operational forces to be white noise uncorrelated sequences, the output PSD matrix $\mathbf{S}^q(\mathrm{i}\omega)$ can be modally decomposed as follows [38]:

$$\mathbf{S}^q\left(\mathrm{i}\omega\right) = \sum_{n=1}^{2N} \frac{\boldsymbol{\psi}_n \boldsymbol{\rho}_n^{\mathrm{T}}}{\mathrm{i}\omega - \lambda_n} + \frac{\boldsymbol{\rho}_n \boldsymbol{\psi}_n^{\mathrm{T}}}{-\mathrm{i}\omega - \lambda_n}, \tag{10}$$

where the operational participation vectors (ORV), Eq. (8), result being a combination of the system modal parameters and the unknown (i.e. forces are not measured) input correlation terms. For this reason, the modal participation factors and by consequence the modal scale factors cannot be determined from a single OMA test but they need appropriate methods for scaling [39].

Usually, the so-called positive power spectra are employed in the output-only identification techniques for their algebraic similarity to FRFs [40]. Indeed, positive power spectra matrix is defined as the Fourier transform of the causal part of the correlation matrix resulting

$$\mathbf{S}^{q+}\left(\mathrm{i}\omega\right) = \sum_{n=1}^{2N} \frac{\boldsymbol{\psi}_n \boldsymbol{\rho}_n^{\mathrm{T}}}{\mathrm{i}\omega - \lambda_n}, \tag{11}$$

or in a compact form

$$\mathbf{S}^{q+}(\mathrm{i}\omega) = \boldsymbol{\Psi}(\mathrm{i}\omega\mathbf{I} - \boldsymbol{\Lambda})^{-1}\mathbf{G}^{\mathrm{T}}, \tag{12}$$

with the $2N$ ORV collected in $\mathbf{G} \in \mathbb{C}^{N\times 2N}$, representing a modal decomposition similar to that of Eq. (2) except for the definition of operational reference vectors $\boldsymbol{\rho}_n$.

2.2 Generalized PSD modal model

In a similar fashion but without making any assumption on the particular structure of $\mathbf{S}^f(\mathrm{i}\omega)$, the output PSD matrix of Eq. (4) can be written in partial fraction by means of the following decomposition [41]

$$\mathbf{S}^q(\mathrm{i}\omega) = \sum_{n=1}^{2N} \frac{\mathbf{R}_n^+(\mathrm{i}\omega)}{\mathrm{i}\omega - \lambda_n} + \frac{\mathbf{R}_n^-(\mathrm{i}\omega)}{-\mathrm{i}\omega - \lambda_n}, \tag{13}$$

where the residue referred to the n-th pole is expressed by

$$\mathbf{R}_n^+(\mathrm{i}\omega) = \boldsymbol{\psi}_n\boldsymbol{\rho}_n(\mathrm{i}\omega)^{\mathrm{T}}, \tag{14}$$

in which the vector $\boldsymbol{\rho}_n(\mathrm{i}\omega)^{\mathrm{T}}$ is defined as

$$\begin{aligned}\boldsymbol{\rho}_n(\mathrm{i}\omega)^{\mathrm{T}} &= \boldsymbol{L}_n^{\mathrm{T}}\mathbf{S}^f(\mathrm{i}\omega)\left(\sum_{s=1}^{2N}\frac{\boldsymbol{L}_s\boldsymbol{\psi}_s^{\mathrm{T}}}{-\lambda_n-\lambda_s}\right) = \\ &= \sum_{s=1}^{2N}\boldsymbol{L}_n^{\mathrm{T}}\mathbf{S}^f(\mathrm{i}\omega)\frac{\boldsymbol{L}_s\boldsymbol{\psi}_s^{\mathrm{T}}}{-\lambda_n-\lambda_s} = \sum_{s=1}^{2N}\frac{\sum_{g=1}^{L}L_{g,n}\sum_{l=1}^{L}S_{gl}^f(\mathrm{i}\omega)L_{l,s}}{-\lambda_n-\lambda_s}\boldsymbol{\psi}_s^{\mathrm{T}} = \sum_{g=1}^{L}\sum_{l=1}^{L}S_{gl}^f(\mathrm{i}\omega)\boldsymbol{g}_n^{gl\mathrm{T}},\end{aligned} \tag{15}$$

where the extended operational reference vector $\boldsymbol{g}_n^{gl}$, related to the input correlation matrix entry $S_{gl}^f(\mathrm{i}\omega)$, occurs as

$$\boldsymbol{g}_n^{gl} = L_{g,n}\sum_{s=1}^{2N}\frac{L_{l,s}}{-\lambda_n-\lambda_s}\boldsymbol{\psi}_s. \tag{16}$$

Analogously, you notice that

$$\begin{aligned}\mathbf{R}_n^-(\mathrm{i}\omega) &= \left(\sum_{s=1}^{2N}\frac{\boldsymbol{\psi}_s\boldsymbol{L}_s^{\mathrm{T}}}{-\lambda_n-\lambda_s}\right)\mathbf{S}^f(\mathrm{i}\omega)\boldsymbol{L}_n\boldsymbol{\psi}_n^{\mathrm{T}} = \\ &= \left(\sum_{s=1}^{2N}\boldsymbol{\psi}_s\frac{\sum_{g=1}^{L}L_{g,s}\sum_{l=1}^{L}S_{gl}^f(\mathrm{i}\omega)L_{l,n}}{-\lambda_n-\lambda_s}\right)\boldsymbol{\psi}_n^{\mathrm{T}} = \\ &= \left(\sum_{g=1}^{L}\sum_{l=1}^{L}S_{lg}^f(-\mathrm{i}\omega)L_{l,n}\sum_{s=1}^{2N}\frac{L_{g,s}}{-\lambda_n-\lambda_s}\boldsymbol{\psi}_s\right)\boldsymbol{\psi}_n^{\mathrm{T}} = \\ &= \left(\sum_{l=1}^{L}\sum_{g=1}^{L}S_{lg}^f(-\mathrm{i}\omega)\boldsymbol{g}_n^{lg}\right)\boldsymbol{\psi}_n^{\mathrm{T}} = \boldsymbol{\rho}_n(-\mathrm{i}\omega)\boldsymbol{\psi}_n^{\mathrm{T}},\end{aligned} \tag{17}$$

and thus Eq. (13) can be written as

$$\mathbf{S}^q(\mathrm{i}\omega) = \sum_{n=1}^{2N}\frac{\boldsymbol{\psi}_n\boldsymbol{\rho}_n(\mathrm{i}\omega)^{\mathrm{T}}}{\mathrm{i}\omega-\lambda_n} + \frac{\boldsymbol{\rho}_n(-\mathrm{i}\omega)\boldsymbol{\psi}_n^{\mathrm{T}}}{-\mathrm{i}\omega-\lambda_n}. \tag{18}$$

In the following, $\boldsymbol{g}_n^{gl}$ is referred to as the extended operational reference vectors (eORV) related to the r-th pole and the gl-th entry of matrix $\mathbf{S}^f(\mathrm{i}\omega)$, while $\boldsymbol{\rho}_n(\mathrm{i}\omega)$ is called frequency dependent ORV (ω-ORV). Similar to the classical operational reference factors, these quantities do not represent a scale factor for the modal shape. The modal decomposition in Eq. (18) can be called the generalized PSD modal model. Differently from the classical PSD modal model, the dependency on the input PSD functions is clarified and no assumptions about the inputs are used to achieve the formulation.

2.3 MPE technique: a two step approach

In the previous section, the modal decomposition of the output PSD matrix is derived referring to a linear, time-invariant, damped, vibrating system having N dofs and subjected to L external forces. If you generalize to the the multi-input, multi-output, and multi-mode case, Eq. (18) can be written into matrix notation as

$$\mathbf{S}^q\left(\mathrm{i}\omega\right) = \boldsymbol{\Psi}(\mathrm{i}\omega\mathbf{I} - \boldsymbol{\Lambda})^{-1}\mathbf{P}(\mathrm{i}\omega)^{\mathrm{T}} + \mathbf{P}(-\mathrm{i}\omega)(-\mathrm{i}\omega\mathbf{I} - \boldsymbol{\Lambda})^{-1}\boldsymbol{\Psi}^{\mathrm{T}}, \tag{19}$$

where $\mathbf{S}^q(\omega) \in \mathbb{C}^{o\times r}$ relates o outputs and r references, $\boldsymbol{\Lambda} \in \mathbb{C}^{2N_p\times 2N_p}$ is a diagonal matrix, containing the $2N_p$ complex conjugate system poles λ_n in the frequency band of interest, while $\boldsymbol{\Psi} \in \mathbb{C}^{o\times 2N_p}$ collects the mode shape vectors and $\mathbf{P}(\mathrm{i}\omega) \in \mathbb{C}^{r\times 2N_p}$ gathers together the ω-ORV being

$$\mathbf{P}(\mathrm{i}\omega) = \sum_{g=1}^{L}\sum_{l=1}^{L} S_{gl}^f\left(\mathrm{i}\omega\right)\mathbf{G}_{gl}, \tag{20}$$

with the $2N_p$ eORV collected in $\mathbf{G}_{gl} \in \mathbb{C}^{r\times 2N_p}$. The output PSD matrix could be considered as $\mathbf{S}^q(\mathrm{i}\omega) = \tilde{\mathbf{S}}^q(\mathrm{i}\omega) + \tilde{\mathbf{S}}^q(\mathrm{i}\omega)^{\mathrm{H}}$, where $\tilde{\mathbf{S}}^q(\mathrm{i}\omega)$ indicates the part of the PSDs related to stable poles. The equivalent matrix polynomial model in the z-domain is derived as

$$\mathbf{S}^q(\omega_k) = \mathbf{D}(k)^{-1}\mathbf{N}^{(e)}(k), \tag{21}$$

with $\mathbf{N}^{(e)}(k) = \sum_{g=1}^{L}\sum_{l=1}^{L} S_{gl}^f(\omega_k)\mathbf{N}^{gl}(k) \in \mathbb{C}^{o\times r}$ here called extended fitting polynomial numerator matrix and $\mathbf{D}(k) \in \mathbb{C}^{o\times o}$ the denominator matrix, whose coefficient matrices represent the parameters to be estimated. Specifically, $\mathbf{N}^{(e)}(k)$ definition incorporates several a-priori known features resulting from loads which explicitly violate the NExT assumption, such as coloured noises, time and spatial correlation among multiple inputs, presence of deterministic loads such as harmonics. One can easily demonstrate how the description in Eq. (21) collapses in the classical LMFD description [40] by imposing the associated to the NExT hypothesis. The polynomial coefficient estimation problem of Eq. (21) can be solved, in a Least-Square sense, with the poly-reference version of the LSCF estimator that differs from the classical one [42] because of the particular matrix description which includes the definition of an extended fitting polynomial numerator matrix $\mathbf{N}^{(e)}(\omega_k)$. Once one determines poles and mode shapes, the remaining unknowns can be estimated with a Least-Squares Frequency-Domain estimator (LSFD) minimizing the scatter between the estimated PSD matrix $\mathbf{S}^q\left(\mathrm{i}\omega\right)$ and the modeled one by exploiting Eq. (19).

3 Applications

In order to validate the two steps MPE procedure previously described, a test case is exploited characterized by a particular the correlation input matrix $\mathbf{S}^f(\mathrm{i}\omega)$. Considering the case of two external loads, $\boldsymbol{f}(t) \in \mathbb{R}^{2\times 1}$, one can generally represent $\mathbf{S}^f(\mathrm{i}\omega) \in \mathbb{C}^{2\times 2}$ as

$$\mathbf{S}^f\left(\mathrm{i}\omega\right) = \begin{bmatrix} S_1\left(\omega\right) & \Gamma\left(\omega\right)\sqrt{S_1\left(\omega\right)S_2\left(\omega\right)}\mathrm{e}^{\mathrm{i}\omega\tau} \\ \Gamma\left(\omega\right)\sqrt{S_1\left(\omega\right)S_2\left(\omega\right)}\mathrm{e}^{-\mathrm{i}\omega\tau} & S_2\left(\omega\right) \end{bmatrix}, \tag{22}$$

where $S_i(\omega)$ is the auto-PSD function referred to i-th force, τ indicates the generic time-lag between two sources, and $\Gamma(\omega)$ stands for the coherence function classically defined as

$$\Gamma\left(\omega\right) = \frac{\left|S_{12}\left(\omega\right)\right|}{\sqrt{S_1\left(\omega\right) S_2\left(\omega\right)}}. \tag{23}$$

In the offered case study we process the time records collected through real-world experiments of MIMO environmental testing, performed on a slender beam of known geometry and material properties, shown in Figure 1. Different infringements of the NExT assumption are investigated by varying the quantities $S_i(\omega)$, τ, $\Gamma(\omega)$ of the PSD matrix in Eq. (22), and so studying the effect of colored noise excitation, temporal correlation and coherence between forces on the OMA procedures. Each of these statistical features is emblematic of the loading environment in which typical mechanical structures (such as vehicles and wind turbines) operate, justifying the need to be gradually tackled by employing an entry-level example, i.e. a discrete system model, and then by approaching an experimental subject. In each application, the first and second step of the identification procedure are carried out by classical and generalized operational modal analysis approach. In Table 1, a comparison is set up between the classical OMA procedure (commercially known as PolyMAX [43]), as a basis for comparison, and the generalized one.

Table 1: Comparison between the two step identification procedures employed in the OMA and G-OMA approach. In the results line, we indicate the modal parameters coming out from each step.

	OMA	G-OMA
1st Step	pLSCF based on RMFD	pLSCF based on eLMFD
MFD	$\mathbf{S}^{q+}(\omega_k) = \mathbf{N}(k)\mathbf{D}(k)^{-1}$	$\mathbf{S}^{q}(\omega_k) = \mathbf{D}(k)^{-1}\mathbf{N}^{(e)}(k)$
Results	$\mathbf{\Lambda}$, $\mathbf{G}$	$\mathbf{\Lambda}$, $\mathbf{\Psi}$
2nd Step	LSFD based on classical half positive PSD modal model	LSFD based on generalized PSD modal model
Modal model	$\mathbf{S}^{q+}\left(\mathrm{i}\omega\right) = \mathbf{\Psi}(\mathrm{i}\omega\mathbf{I} - \mathbf{\Lambda})^{-1}\mathbf{G}^{\mathrm{T}}$	$\mathbf{S}^{q}\left(\mathrm{i}\omega\right) = \mathbf{\Psi}(\mathrm{i}\omega\mathbf{I} - \mathbf{\Lambda})^{-1}\mathbf{P}(\mathrm{i}\omega)^{\mathrm{T}} + +\mathbf{P}(-\mathrm{i}\omega)(-\mathrm{i}\omega\mathbf{I} - \mathbf{\Lambda})^{-1}\mathbf{\Psi}^{\mathrm{T}}$
Results	$\mathbf{\Psi}$	$\mathbf{P}(\omega)$

As one can notice, main differences, regarding the first step, are related to the matrix fraction description used to describe $\mathbf{S}^q(\omega)$, which leads to distinct state-space realization resulting in distinct modal role of the companion matrix eigenvectors (as appreciable in the line of 1st step results). The modal vectors, extracted from the pLSCF algorithm, also depend upon the choice of polynomial basis functions, z_k or z_k^{-1}, which in turn captures the part of $\mathbf{S}^q(\omega)$ bound up with stable poles, $\tilde{\mathbf{S}}^q(\omega)$, or unstable poles, $\tilde{\mathbf{S}}^q(\omega)^{\mathrm{H}}$. In our cases, the option z_k is adopted for both OMA and G-OMA approach. For the experimental case study, positive power spectra are processed with the classical OMA which still employs the RMFD in Table 1 at the first identification step but needs a model model like $\mathbf{S}^{q+}\left(\mathrm{i}\omega\right) = \mathbf{\Psi}(\mathrm{i}\omega\mathbf{I}-\mathbf{\Lambda})^{-1}\mathbf{G}^{\mathrm{T}}$ for the LSFD estimator. In the results discussion, natural frequencies and damping ratios are compared to reference values, the mode shapes are validated by calculating the relevant MAC with respect to a reference modal vector set, and synthesized modal models are compared with measured spectra through synthesis correlation coefficients and normalised errors.

3.1 Experimental case study

In Figure 1, the slender beam used to perform the MIMO environmental testing experiments, is represented. Specifically, the specimen is a PTFE beam of length, width, and thickness equal to $610\,\mathrm{mm}$, $100\,\mathrm{mm}$, and $10\,\mathrm{mm}$, respectively. We adopt a set-up in which free-free boundary conditions are achieved by suspending the beam through extremely flexible elastic cords. The beam is forced by exerting random loads through two modal exciters, acting along the x-direction, attached to the structure through steel stingers and mechanical impedance sensors screw mounted. The output responses are even measured by eight accelerometers,

attached to the beam's center-line, as shown in Figure 1, and by two impedance heads at the driving point locations. These latter sensors also provide the force measurements employed as control signals for the source driving.

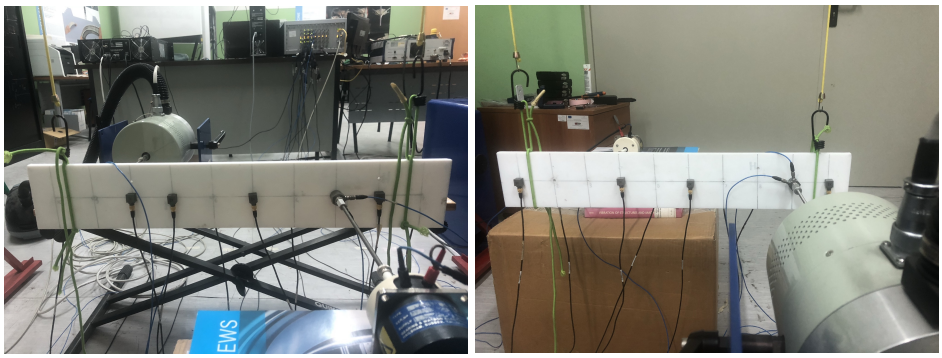

Figure 1: Experimental case study: PTFE beam in free-free boundary conditions. Forces are simulated by two modal shakers attached by stinger.

The experimental setup is, therefore, composed of (i) eight B&K 4535-B-001 triaxial accelerometers, (ii) two PCB 288D01 mechanical impedance sensors, (iii) Dongling ESD-045 and GW-V2/PA30E modal shakers, (iv) a LMS SCADAS III SC310-UTP mobile, equipped with DAC shutdown control box, PC based multichannel analyzer platform, running the LMS Test.Lab 14A software suite for acquiring and recording the time histories of output and input signals, measured by the accelerometers and the impedance head transducers. It is exploited the software module designed for environmental testing specifically for multi-axis random control. By doing so, you are allowed to drive two exciters targeting reference profiles of force PSDs, $S_1^f(\omega)$ and $S_2^f(\omega)$, including also a reference coherence $\Gamma(\omega)$ and a cross-PSD phase angle $\angle S_{12}^f(\omega)$ which determine the cross-correlation term $S_{12}^f(\omega)$, as described in Eq. (22). One loading case is explored represented in Figure 2 which aims at introducing three different infringements of NExT assumption.

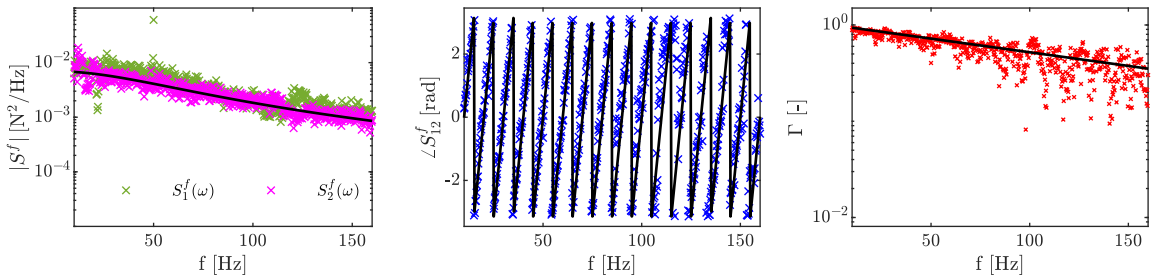

(a) Temporal correlation, coloration, and coherence: $S_1^f(\omega) = S_2^f(\omega) = \dfrac{S_0}{\omega^2 + \omega_0^2}$, $\angle S_{12}^f(\omega) = \omega\tau$, and $\Gamma(\omega) = \mathrm{e}^{-\alpha|\omega|}$

Figure 2: Experimental case study: loading case under no-NExT hypothesis. The dotted coloured lines display quantities derived from impedance head force measurements. On the other hand, black lines show the chosen target profiles whose analytical expression is reported in captions.

Signals are acquired in the time domain, adopting a sampling frequency, a time period, and a number of repetitions equal to $800\,\mathrm{Hz}$, $4\,\mathrm{s}$, and $M = 50$, respectively. Figure 3 offers the magnitude of cross-PSD between the 10^{th} and 5^{th} acceletometer signals, obtained by processing the system responses by means of the weighted correlogram when a 0.001% exponential window is applied.

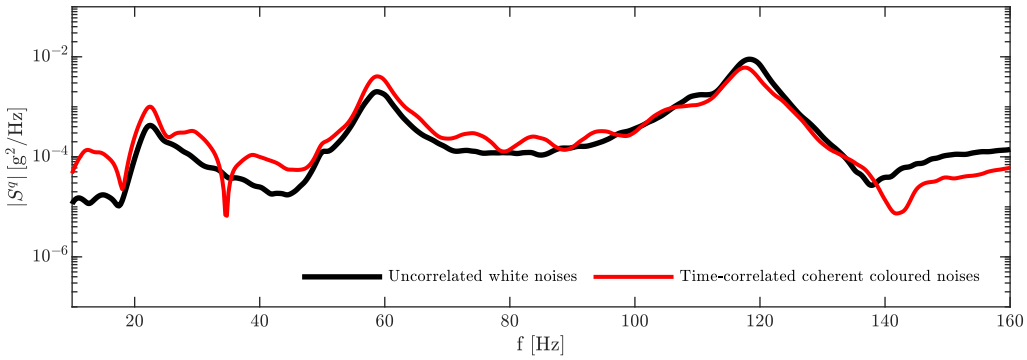

Figure 3: Experimental case study: magnitude of output crossPSD relating the 10^{th} and 5^{th} acceleration signals. The classical NExT loading case, black line, is compared with the No-NExT loading cases, described in Figure 2, where temporal correlation, coloration, and coherence between forces is introduced, red line.

The time delay between the loads, acting at the 3^{rd} and 9^{th} location, introduces humps in the magnitude of the cross-PSDs, see the relevant distortion comparing the black line, referred to uncorrelated white noises case, and the red one, where temporal correlation is reproduced. The coloration effect arises looking at the energy distribution in frequency. Coherence between the excitations, simulated according to an exponential law, produces the expected attenuation of humps with increasing frequency.

Table 2: PTFE beam system: natural frequencies and damping ratios extracted by classical modal analysis techniques [44].

	Natural Frequency (Hz)	Damping Ratio (%)
Mode 1	22.1102	1.9463
Mode 2	58.5501	2.0002
Mode 1T	109.655	1.4797
Mode 3	117.967	1.4875

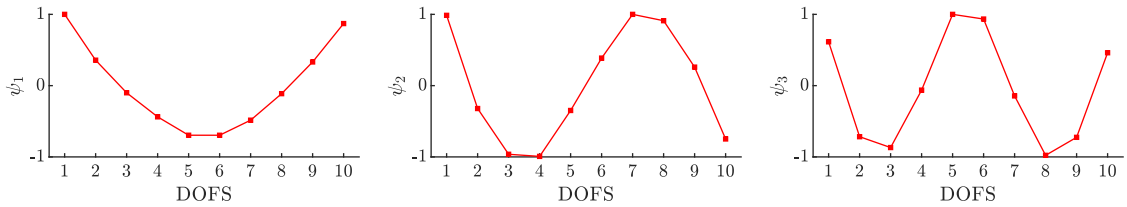

Figure 4: PTFE beam system: mode shapes extracted by classical modal analysis techniques. Blue dots: underformed nodes; red squares: deformed nodes.

In the following sections, the identification procedure is performed operating in the frequency band $10-160$ Hz that contains the first three flexural modes (along with a torsional one, around 110 Hz, which further emerges in some loading conditions despite sensor and force locations) extracted by classical modal analysis techniques [44] and collected in Table 2 and Figure 4.

3.1.1 First identification step: pLSCF

The three no-NExT effects here investigated are combined. So, in this loading condition the designed $\mathbf{N}^{(e)}(\omega)$ includes the knowledge of the temporal delay τ together with the frequency dependence of coloration and coherence models.

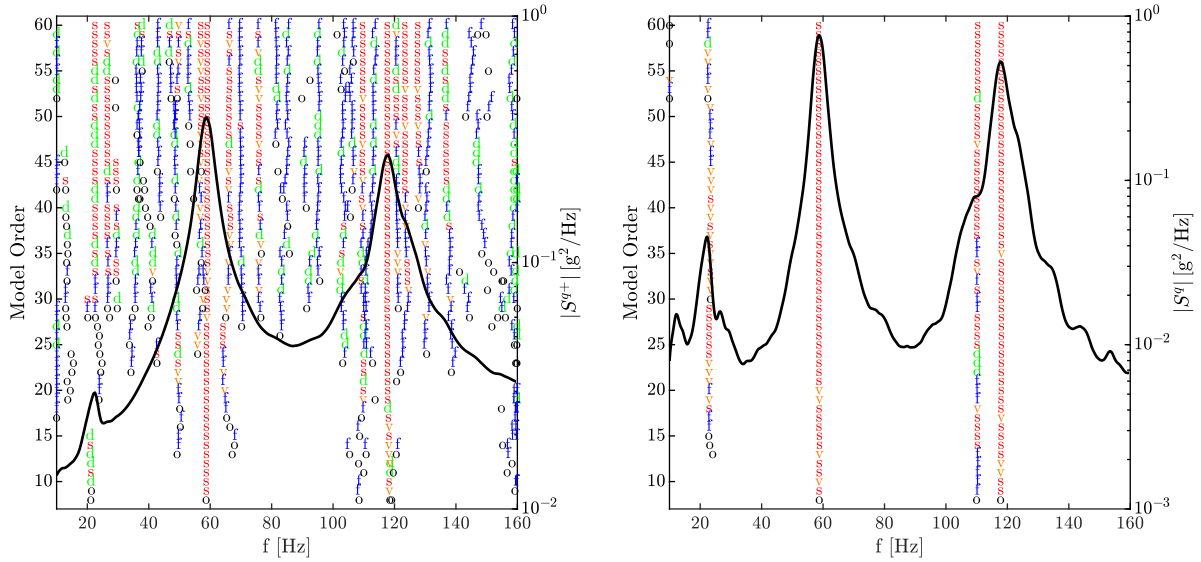

(a) OMA (b) G-OMA

Figure 5: Identification of the experimental system: stabilisation diagram along with the magnitude of the PSDs sum function, blue dotted line. The model order is indicated on the left ordinate axis. 'o': new pole; 'f' stabilisation in natural frequency; 'f' extra stabilisation in damping ratio; 'v' extra stabilisation in MAC value; 's' full stabilisation. Stabilisation thresholds for natural frequency, damping ratio, and MAC value are 1%, 5%, and 2%, respectively.

The two stabilisation diagrams in Figure 5 reveal different clarity highlighting the more accuracy of the G-OMA approach. The effect of coherence is reversed into the presence of a fourth peak, see Figure 5b, related to the first torsional mode of the PTFE beam, that result more excited when the two loads loose correlation (as it happens at high frequency due to the effect of the coherence term $\mathrm{e}^{-\alpha|\omega|}$). By looking at Figure 5a, pole selection is still quite challenging due to the stabilisation lines related to spurious mathematical poles deriving from the violation of the NExT assumption. By forcing selection in correspondence of the expected natural frequencies for the OMA stabilisation diagram, a comparison of the MPE results is established in Table 3 and Figure 6. The proposed identification procedure generally offers a better estimation for both frequencies and damping ratios as confirmed by the error values. Worse results are reached for the less excited modes, first flexural and torsional ones, because of the measurement noise effect. The MAC values reveal similar performances in terms of mode shapes estimate and they confirm the poor observability of the torsional mode related to force and sensor locations.

Table 3: Comparison between exact and estimated natural frequencies. Estimates computed by using classical and generalized OMA formulations are compared. Percentage relative error, $\Delta = 100 \times (v_{\text{ref}} - v_{\text{est}})/v_{\text{ref}}$, with respect to reference value is reported nearby each estimate.

		Natural Frequency (Hz)		Damping Ratio (%)	
		Estimated	$\lvert\Delta\rvert$(%)	Estimated	$\lvert\Delta\rvert$(%)
OMA	Mode 1	22.4837	1.6893	5.1303	163.5944
	Mode 2	59.0800	0.9050	2.9887	49.4195
	Mode 1T	109.5787	0.0696	1.6697	12.8399
	Mode 3	117.6550	0.2645	2.0689	39.0821
G-OMA	Mode 1	22.5279	1.8890	0.9353	51.9459
	Mode 2	58.8164	0.4548	2.2579	12.8852
	Mode 1T	110.0922	0.3987	1.0549	28.7080
	Mode 3	117.9556	0.0097	1.3484	9.3519

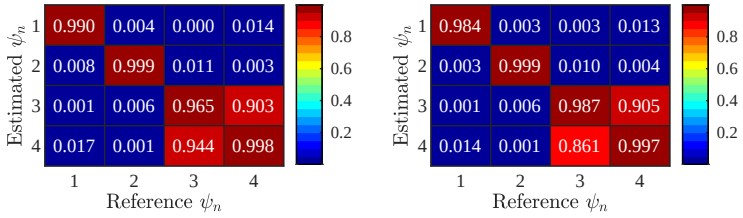

(a) OMA (b) G-OMA

Figure 6: MAC between reference and estimated modal vectors' sets estimated by following (a) the classical OMA procedure and (b) the generalized approach proposed in the paper.

3.1.2 Second identification step: LSFD

This last loading case is characterized by the frequency-dependent operational reference vector $\boldsymbol{\rho}_n(\mathrm{i}\omega)$ which embeds some a priori known features regarding input correlation and coloration, such as the temporal delay τ and the frequency dependence of coloration and coherence models. It is highlighted the suitability of the G-OMA method emphasised by low errors, below 5%, and high correlation coefficients, greater than 95%, as confirmed by the visual match in Figure 7(b). Furthermore, the classical LSFD shortcomings relapse into slightly greater errors, whereas the poles' selection is enforced having poor stabilization charts.

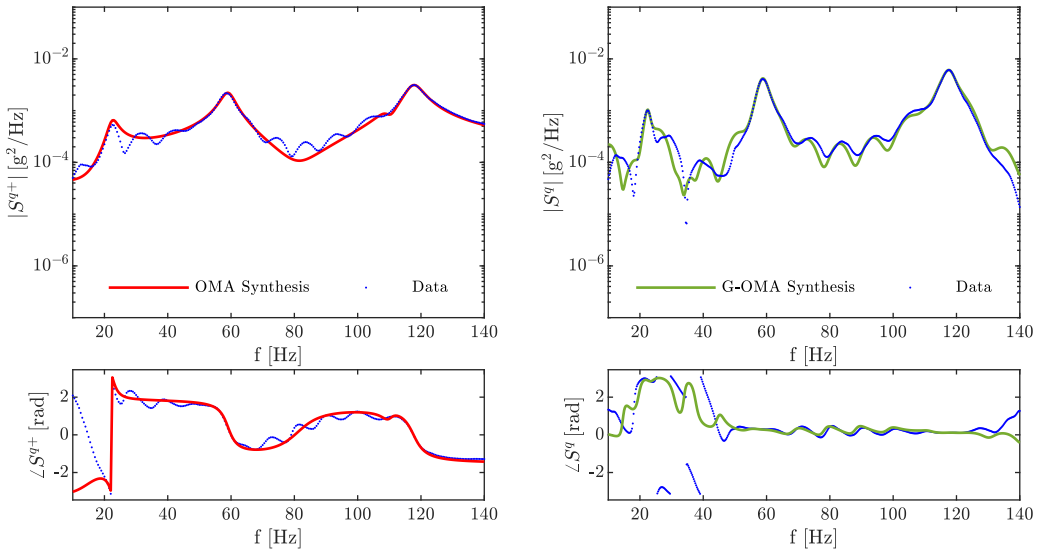

(a) OMA (b) G-OMA

Figure 7: Experimental beam under temporal-correlated colored coherent noises: (a) comparison between one measured positive power spectrum, blue dotted line, and the relevant synthesis obtained by the OMA modal model, red solid line; (b) G-OMA modal model synthesis, green solid line, of one measured output PSD, blue dotted line. The chosen matrix entry relates the 10^{th} and 5^{th} accelerations in the both plots.

4 Conclusions

This work outlines the development of a generalized OMA framework, meaning an alternative approach aiming at overcoming the NExT assumption limitations, which occur when output-only modal analysis is performed on mechanical system, such as vehicles during road test or operating wind turbines. The G-OMA approach is designed to fix no-NExT effects (i.e. coloration, time correlation, coherence, harmonics, etc.) by including a priori known input correlation features in OMA modal structures. In fact, a generalized modal decomposition of CFs and PSDs matrix is clarified by making no assumptions about the forces correlation. In doing so, the concept of frequency (or time lag) dependent operational reference vectors arises as a class of modal vectors which in turn collects a combination of several contributions related to the forces acting on the system. Moving from the theoretical generalized PSD partial fraction decomposition, a specific two step identification procedure, operating in the frequency domain, is developed. The first step, resulting in poles and mode shapes estimation, is based upon an extended left matrix fraction description and its relevant state-space observable canonical realization. The second step is an LSFD-based estimator operating on the extended operational reference vectors calculation. The investigated no-NExT effects are the coloured nature of stochastic loads, the presence of temporal correlation and coherence between inputs. The proposed formulation is compared with the classical one by performing modal parameter estimation of an experimental PTFE beam under different operating loading conditions, comprising a number of NExT assumption infringements. The suitability of the G-OMA method is confirmed by improved results in terms of stabilisation diagram and modal parameters accuracy. The usage of identification techniques, based on the modal structures here proposed, could inspire simple and cost-effective “ad hoc” tools able to compute the modal parameters of mechanical systems under operating conditions that violate to a certain extent the hypothesis of the classical OMA techniques.

References

[1] X. Lu, X. He, H. Chen, and R. Zheng, "Operational modal parameter identification with colored noise excitation," *Chinese Journal of Aeronautics*, vol. 34, no. 2, pp. 288–300, 2021. [Online]. Available: https://doi.org/10.1016/j.cja.2020.09.006

[2] C. J. Dodds and J. D. Robson, "The description of road surface roughness," *Journal of Sound and Vibration*, vol. 31, no. 2, pp. 175–183, 1973. [Online]. Available: http://dx.doi.org/10.1016/S0022-460X(73)80373-6

[3] P. Andrén, "Power spectral density approximations of longitudinal road profiles," *International Journal of Vehicle Design*, vol. 40, no. 1-3, pp. 2–14, 2006.

[4] K. Bogsjö, "Evaluation of stochastic models of parallel road tracks," *Probabilistic Engineering Mechanics*, vol. 22, no. 4, pp. 362–370, 2007.

[5] K. Bogsjö, "Coherence of road roughness in left and right wheel-path," *Vehicle System Dynamics*, vol. 46, no. SUPPL.1, pp. 599–609, 2008.

[6] K. Bogsjö, K. Podgórski, and I. Rychlik, "Models for road surface roughness," *Vehicle System Dynamics*, vol. 50, no. 5, pp. 725–747, 2012.

[7] T. Carne and G. James III, "The inception of oma in the development of modal testing technology for wind turbines," *Mechanical Systems and Signal Processing*, vol. 24, no. 5, pp. 1213–1226, 2010.

[8] C. J. Dodds and J. D. Robson, "Partial coherence in multivariate random processes," *Journal of Sound and Vibration*, vol. 42, pp. 243–249, 1975.

[9] K. Song, X. Chen, and Y. Lin, "Wheelbase filtering effect on vehicle ride dynamics," in *Proceedings of the FISITA 2012 World Automotive Congress*. Springer, 2013, pp. 1183–1195.

[10] G. De Filippis, D. Palmieri, L. Soria, L. Mangialardi, B. Peeters, and H. Van der Auweraer, "Operational modal analysis of passenger cars: Effect of the correlation between front and rear inputs," in *Proceedings of the 11th International Conference on Recent Advances in Structural Dynamics (RASD), Pisa, Italy*, 1st–3rd July 2013.

[11] M. S. Allen, M. W. Sracic, S. Chauhan, and M. H. Hansen, "Output-only modal analysis of linear time-periodic systems with application to wind turbine simulation data," *Mechanical Systems and Signal Processing*, vol. 25, no. 4, pp. 1174–1191, 2011.

[12] F. B. Zahid, Z. C. Ong, and S. Y. Khoo, "A review of operational modal analysis techniques for in-service modal identification," *Journal of the Brazilian Society of Mechanical Sciences and Engineering*, vol. 42, no. 8, pp. 1–18, 2020. [Online]. Available: https://doi.org/10.1007/s40430-020-02470-8

[13] R. Brincker, P. Andersen, and N. Moller, "Indicator for separation of structural and harmonic modes in output-only modal testing," *Proceedings of the International Modal Analysis Conference - IMAC*, vol. 2, pp. 1649–1654, 2000.

[14] R. B. Randall and W. A. Smith, "New cepstral techniques for operational modal analysis," in *WCCM 2017 - 1st World Congress on Condition Monitoring 2017*, 2017.

[15] R. B. Randall, J. Antoni, and W. A. Smith, "A survey of the application of the cepstrum to structural modal analysis," *Mechanical Systems and Signal Processing*, vol. 118, pp. 716–741, 2019. [Online]. Available: https://doi.org/10.1016/j.ymssp.2018.08.059

[16] S. Gres, P. Andersen, C. Hoen, and L. Damkilde, "Orthogonal projection-based harmonic signal removal for operational modal analysis," in *Conference Proceedings of the Society for Experimental Mechanics Series*, vol. 6, 2019, pp. 9–21.

[17] P. Mohanty and D. Rixen, "Operational modal analysis in the presence of harmonic excitation," *Journal of Sound and Vibration*, vol. 270, pp. 93–109, 2004.

[18] P. Mohanty and D. J. Rixen, "Modified ERA method for operational modal analysis in the presence of harmonic excitations," *Mechanical Systems and Signal Processing*, vol. 20, pp. 114–130, 2006.

[19] C. Devriendt, G. De Sitter, S. Vanlanduit, and P. Guillaume, "Operational modal analysis in the presence of harmonic excitations by the use of transmissibility measurements," *Mechanical Systems and Signal Processing*, vol. 23, no. 3, pp. 621–635, 2009.

[20] W. Weijtjens, G. De Sitter, C. Devriendt, and P. Guillaume, "Automated transmissibility based operational modal analysis for continuous monitoring in the presence of harmonics," *Proceedings of the International Conference on Structural Dynamic , EURODYN*, vol. 2014-Janua, no. July, pp. 2231–2238, 2014.

[21] P. Guillaume, T. De Troyer, C. Devriendt, and G. De Sitter, "OMAX - A combined experimental-operational modal analysis approach," in *Proceedings of ISMA2006: International Conference on Noise and Vibration Engineering*, vol. 5, 2006, pp. 2985–2996.

[22] E. Reynders and G. D. Roeck, "Reference-based combined deterministic-stochastic subspace identification for experimental and operational modal analysis," *Mechanical Systems and Signal Processing*, vol. 22, no. 3, pp. 617–637, 2008.

[23] E. Reynders, D. Degrauwe, M. Schevenels, G. De Roeck, P. Van den Broeck, K. Deckers, and P. Guillaume, "OMAX testing of a steel bowstring footbridge," in *Conference Proceedings of the Society for Experimental Mechanics Series 7*, vol. 4, 2011, pp. 357–364. [Online]. Available: http://www.springerlink.com/index/10.1007/978-1-4419-9316-8

[24] J. Antoni and S. Chauhan, "A study and extension of second-order blind source separation to operational modal analysis," *Journal of Sound and Vibration*, vol. 332, no. 4, pp. 1079–1106, 2013. [Online]. Available: http://dx.doi.org/10.1016/j.jsv.2012.09.016

[25] I. G. Araújo, J. A. G. Sánchez, and P. Andersen, "Modal parameter identification based on combining transmissibility functions and blind source separation techniques," *Mechanical Systems and Signal Processing*, vol. 105, pp. 276–293, 2018.

[26] G. Sternharz and T. Kalganova, "Current methods for operational modal analysis of rotating machinery and prospects of machine learning," *Conference Proceedings of the Society for Experimental Mechanics Series*, vol. 6, pp. 155–163, 2020.

[27] D. Tcherniak, S. Chauhan, and M. H. Hansen, "Applicability limits of operational modal analysis to operational wind turbines," in *Conference Proceedings of the Society for Experimental Mechanics Series*, vol. 1, 2011, pp. 317–327.

[28] P. Skjoldan and M. Hansen, "On the similarity of the coleman and lyapunov-floquet transformations for modal analysis of bladed rotor structures," *Journal of Sound and Vibration*, vol. 327, no. 3-5, pp. 424–439, 2009.

[29] L. Soria, B. Peeters, and J. Anthonis, "Operational Modal Analysis and the performance assessment of vehicle suspension systems," *Shock and Vibration*, vol. 19, no. 5, pp. 1099–1113, 2012.

[30] M. Rezaee, V. Shaterian-Alghalandis, and A. Banan-Nojavani, "Development of the smooth orthogonal decomposition method to derive the modal parameters of vehicle suspension system," *Journal of Sound and Vibration*, vol. 332, no. 7, pp. 1829–1842, 2013.

[31] X. Dong, J. Lian, M. Yang, and H. Wang, "Operational modal identification of offshore wind turbine structure based on modified stochastic subspace identification method considering harmonic interference," *Journal of Renewable and Sustainable Energy*, vol. 6, no. 3, 2014.

[32] G. De Filippis, D. Palmieri, L. Soria, and L. Mangialardi, "System and source identification from operational vehicle responses: A novel modal model accounting for the track-vehicle interaction," *arXiv e-prints*, p. arXiv:1702.08325, 2017.

[33] G. De Filippis, L. Mangialardi, D. Palmieri, and L. Soria, "Method for determining the modal parameters of road or rail vehicles and for the indirect characterization of road or rail profiles," 2017.

[34] S. De Carolis, G. De Filippis, D. Palmieri, and L. Soria, "A generalized operational modal analysis framework for challenging no-next engineering applications," 2020, p. 1819 – 1832.

[35] S. De Carolis, G. De Filippis, D. Palmieri, and L. Soria, "Operational-modal-analysis-based processing of no-next engineering applications datasets: A generalized power spectral density modal model formulation," 2021.

[36] W. Heylen, S. Lammens, and P. Sas, *Modal Analysis Theory and Testing*. Katholieke Universteit Leuven, Departement Werktuigkunde, 2007.

[37] D. Newland, *An introduction to random vibrations, spectral and wavelet analysis*. Longman Scientific & Technical (Harlow, Essex, England and New York), 1993.

[38] F. Shen, M. Zheng, D. Feng Shi, and F. Xu, "Using the cross-correlation technique to extract modal parameters on response-only data," *Journal of Sound and Vibration*, vol. 259, no. 5, pp. 1163–1179, 2003.

[39] P. Fernández, P. Reynolds, and M. López-Aenlle, "Scaling mode shapes in output-only systems by a consecutive mass change method," *Experimental Mechanics*, vol. 51, no. 6, pp. 995–1005, 2011.

[40] E. Reynders, J. Houbrechts, and G. De Roeck, "Fully automated (operational) modal analysis," *Mechanical Systems and Signal Processing*, vol. 29, pp. 228–250, 2012. [Online]. Available: http://dx.doi.org/10.1016/j.ymssp.2012.01.007

[41] B. Peeters, "System identification and damage detection in civil engineering," Ph.D. dissertation, Katholieke Universiteit Leuven, Belgium, 2000.

[42] P. Guillaume, P. Verboven, S. Vanlanduit, H. Van der Auweraer, and B. Peeters, "A poly-reference implementation of the least-squares complex frequency-domain estimator," *Proceedings of IMAC*, vol. 21, 01 2003.

[43] B. Peeters, H. Van Der Auweraer, P. Guillaume, and J. Leuridan, "The PolyMAX frequency-domain method: A new standard for modal parameter estimation?" *Shock and Vibration*, vol. 11, no. 3-4, pp. 395–409, 2004.

[44] P. Verboven, P. Guillaume, B. Cauberghe, S. Vanlanduit, and E. Parloo, "A comparison of frequency-domain transfer function model estimator formulations for structural dynamics modelling," *Journal of Sound and Vibration*, vol. 279, no. 3-5, pp. 775–798, 2005.